# Frequency bandwidth extension by use of multiple Zeeman field offsets for electron spin-echo EPR oxygen imaging of large objects

Payam Seifi, Boris Epel, Subramanian V. Sundramoorthy, Colin Mailer, and Howard J. Halpern[a)]
*Department of Radiation and Cellular Oncology, Center for EPR Imaging In Vivo Physiology, The University of Chicago, Chicago, Illinois 60637*

(Received 7 September 2010; revised 20 April 2011; accepted for publication 21 April 2011; published 31 May 2011)

**Purpose:** Electron spin-echo (ESE) oxygen imaging is a new and evolving electron paramagnetic resonance (EPR) imaging (EPRI) modality that is useful for physiological *in vivo* applications, such as EPR oxygen imaging (EPROI), with potential application to imaging of multicentimeter objects as large as human tumors. A present limitation on the size of the object to be imaged at a given resolution is the frequency bandwidth of the system, since the location is encoded as a frequency offset in ESE imaging. The authors' aim in this study was to demonstrate the object size advantage of the multioffset bandwidth extension technique.
**Methods:** The multiple-stepped Zeeman field offset (or simply multi-B) technique was used for imaging of an 8.5-cm-long phantom containing a narrow single line triaryl methyl compound (trityl) solution at the 250 MHz imaging frequency. The image is compared to a standard single-field ESE image of the same phantom.
**Results:** For the phantom used in this study, transverse relaxation ($T_{2e}$) electron spin-echo (ESE) images from multi-B acquisition are more uniform, contain less prominent artifacts, and have a better signal to noise ratio (SNR) compared to single-field $T_{2e}$ images.
**Conclusions:** The multi-B method is suitable for imaging of samples whose physical size restricts the applicability of the conventional single-field ESE imaging technique. © *2011 American Association of Physicists in Medicine*. [DOI: 10.1118/1.3590365]

Key words: electron paramagnetic resonance, electron spin-echo imaging, frequency bandwidth, large object, multi-B, radiofrequency

## I. INTRODUCTION

Electron spin-echo (ESE) imaging is a time-domain electron paramagnetic resonance (EPR) modality that is capable of acquiring quantitative *in vivo* oxygen images,[1,2] besides other pulse EPR oxygen imaging (EPRI) techniques.[3,4] Due to size limitations, *in vivo* EPR imaging (continuous-wave or pulse) has traditionally been used for oxygen or redox status imaging of tumors or hearts in small rodents, typically mice and rats;[5–12] although tumors grown in rabbits, which are similar in size to those in humans, have also been studied in recent years.[13] Trityl distribution images of a whole mouse have also been acquired by use of free induction decay (FID)-based time-domain EPR imaging.[14,15]

In the case of ESE imaging, one also has to face the issue of the frequency bandwidth of the imager transmitter and receiver arms. Applied field gradients encode the object's spatial information into signal frequency offsets. Therefore, a finite imaging bandwidth is equivalent to a limit on the object size for a given maximum gradient size, or vice versa. For continuous-wave EPR imaging, larger objects simply require proportionally larger magnetic field sweeps for a given gradient. This is a more straight-forward solution,[16] although time-domain techniques have a generally superior SNR acquired per unit time compared to continuous-wave EPR in imaging of trityls.

We have demonstrated that the multiple-stepped Zeeman field offset (multi-B) technique for extending the imager frequency bandwidth can be used for acquisition of images with larger gradient magnitudes, therefore improving the spatial resolution of the ESE image.[17] Artifacts from frequency data truncation and noise amplification were shown to be minimized in this study as well. In this work, we describe how the multi-B technique can be applied to image objects with spatial dimensions comparable to those of human tumors.

In contrast to our high resolution study, different hardware and operating conditions were necessary for the large object study. A large resonator to accommodate the phantom was necessary for this study. Significantly higher power was necessary to precess spin magnetizations by appropriate angles. The nonuniformity of the pulse radiofrequency field over the larger dimensions of the resonator is a complicating factor. Extending the conventional single-field spin-echo technique to objects with a field gradient multiplied by the object size exceeding the imager frequency bandwidth will significantly degrade the image quality, as we will show. The use of multi-B in spin-echo EPRI can therefore be interpreted as equivalent to extending field sweeps in the case of continuous-wave EPRI. The major difference here is that the multifield extension is done in discrete steps where data from different field offsets (i.e., subprojections) overlap.

This overlap is taken into account, as described below, in optimal restoration of complete projections.

One of the major goals of EPR imaging is quantitative oximetry in human tumors. The work presented in this article provides a proof of the principle that the size limitation of the electron spin-echo imaging technique can be resolved, as far as the imaging bandwidth and required pulse radiofrequency power are concerned. This is not a trivial extension of the enhanced-resolution application of multiple Zeeman field offset ESE images, given the different hardware and operational conditions. Compared to the single-field ESE imaging, the multi-B technique produces images with twice better $T_{2e}$ (and oxygen) resolution and drastic reduction in image artifacts, while requiring no major modification in imaging instruments or the acquisition time. This increase in object size is crucial for the extension of the ESE imaging technique to large animals, ultimately aiming toward EPR oxygen imaging of human tumors.

## II. METHODS

### II.A. Imaging phantom

An 8.5-cm-long borosilicate glass tube phantom [Fig. 1(a)] with an inner diameter of 15 mm, partially filled with 200 $\mu$M aqueous solution of deoxygenated, perdeuterated "Finland" triaryl methyl (trityl, or TAM) radical (methyl-tris [8-carboxy-2,2,6,6-tetrakis[perdeuteromethyl] benzo [1,2-d:4,5-d′] bis[1,3] dithiol-4-yl]-trisodium salt [Fig. 1(b)], GE Healthcare, London, UK),[18–20] was used in this study. The phantom was prepared by deoxygenating of the solution with five freeze-pump-thaw cycles and flame-sealing of the glass tube afterward. The phantom was placed horizontally inside the resonator during imaging.

### II.B. RF resonator

A 75-mm-long cylindrical, one loop-one gap resonator with capacitive coupling,[21] with an inner diameter of 25 mm, was used for our ESE imaging experiments [Fig. 1(c)]. The resonator body is made from acrylonitrile butadiene styrene (ABS) plastic coated with ~12.5 $\mu$m of copper and flashed with 2 $\mu$m of gold (General Super Plating, East Syracuse, NY). The quality factor ($Q$) of the resonator was reduced from the original value of 185 suitable for continuous-wave EPR imaging to 19.5 for multi-B ESE and 8.3 for single-B ESE imaging experiments. Lowering of the quality factor was achieved by installation of a 200 Ω ($Q \approx 19.5$) and a 500 Ω ($Q \approx 8.3$) shunt resistor across the resonator capacitor plates for single-B and multi-B experiments, respectively. The resonator $Q$ for the single-B experiment had to be low enough in order to provide sufficient imaging bandwidth, yet high enough so that we could apply short excitation and refocusing RF pulses with the available maximum pulse power from the pulse amplifier (1 KW). Note that using the multi-B technique, the resonator $Q$ did not have to be lowered to the extent of single-B image acquisition, recovering some of the signal-to-noise lost in partial object coverage.

### II.C. EPR imager

Our multipurpose EPR imaging system operating at the 250 MHz central frequency is fully explained in a previous publication.[22] Changes in the transmitter-receiver switch box allowing use of equal-time 90° ($\pi/2$, excitation) and 180° ($\pi$, refocusing) pulses are documented by Sundramoorthy *et al.*[23] (See also Quine *et al.*[24]). To maintain optimized pulse bandwidth in the single-B experiment, we used short high-bandwidth 35 ns pulses. Longer 65 ns pulses were used for the multi-B experiment. This reduced the power necessary and, to some extent, the high-power-induced artifacts. The operation frequency of the imager was adjusted from 250 MHz to the peak absorption frequency of the loaded resonator for each imaging experiment, varying typically 10–15 MHz.

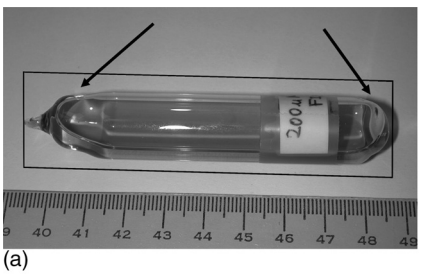

(a)

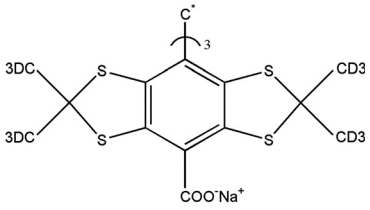

(b)

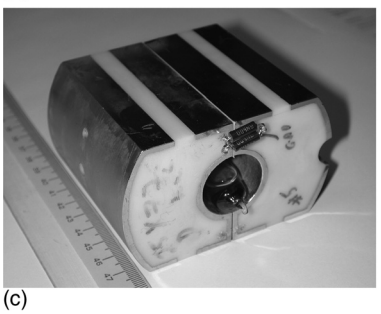
(c)

FIG. 1. (a) The 200 $\mu$M deuterated Finland trityl phantom used for imaging experiments. Black arrows indicate liquid surface menisci at the two ends of the phantom. The rectangle indicates a vertical plane passing through the phantom center axis, corresponding to slices shown in Figs. 3(a)–3(d). (b) Structure of the symmetric Finland molecule. Only one of the three aromatic groups surrounding the paramagnetic carbon center is shown. CD3 indicates perdeuterated methyl group. (c) The resonator used for ESE imaging experiments, with the 500 Ω equivalent shunt resistor (two 1 KΩ resistors in parallel) installed across the resonator gap. Once installed in the magnet, the capacitor plates on top provide coupling to the excitation/detection system. The phantom is placed inside the resonator loop.

TABLE I. The acquisition setting for ESE imaging.

| Parameter | | Protocol | |
|---|---|---|---|
| | | Single-B | Multi-B |
| Acquisition time | Total | 53.3 min | 40.6 min |
| | Pure[a] | 34.9 min | 34.9 min |
| RF power | Peak | 1 KW (60 dBm) | 251 W (54 dBm) |
| | Average | 2.43 W | 1.13 W |
| Pulse length | | 35 ns | 65 ns |
| Echo times ($\tau$) | | Five $\tau$ values, logarithmically spaced: 0.7, 1.05, 1.57, 2.34, 3.5 ($\mu$s) | (Same as single-B) |
| Repetition times | | 18 $\mu$s | 18 $\mu$s |
| Field offsets | | None | 7 offsets, linearly spaced: $-300$, $-200$, $-100$, 0, 100, 200, 300 ($\mu$T) |
| Echo averaging | | 112 000 per projection | 112 000 per complete projection |
| Applied gradient | | 10 mT/m | 10 mT/m |
| Angular sampling, (spatially uniform) (Ref. 32) | | 208 | 208 (1456 subprojections) |
| Baseline acquisition | | Once every two projections (105 baselines) | Once every two complete projections (105 baselines) |
| Imaging bandwidth (FWHM) | | 12.4 MHz | 7.3 MHz (22.3 MHz after multi-B extension) |
| Resonator central frequency | | 235 MHz | 239 MHz |

[a]Pure acquisition time does not take into account the field-switching times and baseline acquisition. Therefore, is equal to (pulse sequence duration) × (number of echo averages) × (number of projections) × (number of echo times).

### II.D. Data acquisition and image reconstruction

Image acquisition parameters for single and multi-B protocols are presented in Table I.

The system acquisition window function (AWF) was measured before each imaging experiment. The AWF, or imager frequency profile, is a measure of the effectiveness with which different frequency components of the signal are detected. In principle the bandwidth of the imager could be estimated using empirical formulas based on pulse length, resonator Q, and individual detection component bandwidths; however, the AWF was more accurately obtained by directly measuring maximum spin-echo signal intensity at varying Zeeman field offsets in the absence of any applied field gradients.[22] The imager AWFs for the single-B and multi-B acquisitions are shown in Fig. 2. Note that the single-B AWF is wider than the individual field step AWF in multi-B, due to the former's lower Q and shorter pulse length. Multi-B effective bandwidth expansion is achieved by application of seven Zeeman field offsets covering from $-300$ micro-Tesla ($\mu$T) to $+300$ $\mu$T, moving the resonance frequency position. The increase in effective frequency bandwidth extends from an initial full-width half-maximum (FWHM) value of 7.3 MHz to 22.3 MHz. Imaging conditions used in the comparison were optimized for each technique to demonstrate the best images obtainable in each case in similar acquisition times.

The multi-B data acquisition and processing of subprojections for recovery of complete projections were described previously.[17] Briefly, for each magnetic field gradient direction, or projection, the electron spin-echo detection is performed at multiple different Zeeman field offsets. The echo signal for each Zeeman field offset contains information from different regions of the projection in the frequency space. For recovering the complete projection, subprojections from these different field offsets are shifted back in the frequency space, proportional to the field offset. In their overlap regions, the subprojections are combined in such a manner as to maximize the SNR at each frequency bin.[17,25] The result is the expansion of the effective imager AWF in frequency space, as illustrated in Fig. 2.

We used the multistage filtered back-projection reconstruction technique to reconstruct all spatial images from projections, where a N (three) dimensional image is

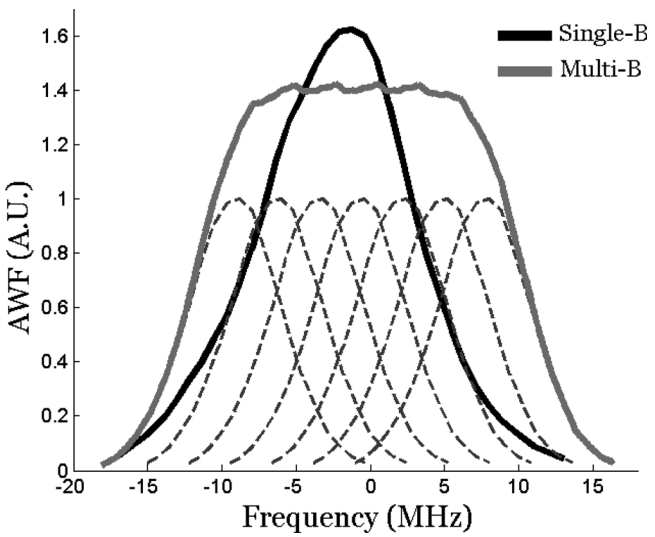


FIG. 2. Expansion of the frequency bandwidth in the multi-B scheme. The black solid line indicates the single-B AWF. Dashed curves represent individual field step AWFs for the multi-B acquisition. The heights are normalized with respect to the square root of the number of averages for each scheme. The extended multi-B bandwidth (gray solid curve) is calculated from individual field steps by the sum of squares (SoS) method.[25]

TABLE II. Image reconstruction information.

| Reconstruction parameter | Value |
|---|---|
| Reconstruction algorithm | Filtered back-projection, two stages |
| Matrix size | 128 × 128 × 128 (×5 echo times) |
| Image field of view | 10 cm |
| Voxel size | 0.78 mm |
| Reconstruction filter | Ram-Lak filter, cutoff at half sampling frequency |
| Angular interpolation | Factor 4, cubic spline interpolation |

reconstructed in N-1 (two) two-dimensional filtered back-projection steps in order to save computation time.[26,27] Relevant image reconstruction parameters are given in Table II.

### II.E. Generating $T_{2e}$ images

As explained by Epel *et al.*[22] and Seifi *et al.*,[17] for each image voxel, a least-squares exponential function was fitted to the five intensity values of each voxel obtained at five echo times. The exponential time constant was the estimated transverse magnetization relaxation time ($T_{2e}$) within each image voxel. We used the fminsearch function in MATLAB (The Mathworks, Natick, MA 01760) to find the best exponential fit. The routine is based on the Nelder–Mead unconstrained nonlinear minimization.[28]

An image mask for exponential fitting was selected: only image voxels with first tau intensities above 15% of the maximum voxel intensity were chosen for fitting. The 15% threshold is routinely used in our *in vivo* EPR experiments; it is high enough to reduce contributions from noise in otherwise empty voxels located outside the phantom or animal body, and low enough to avoid signal voids in animal tissue and tumors, and it provides an outline of the image consistent with registered $T_2$-weighted anatomic NMR images.

### II.F. Determining the $T_{2e}$ uncertainty

The $T_{2e}$ uncertainty was estimated from images of the same trityl phantom in the following manner: once the 15% threshold mask for the image was determined, the two outer layers of the threshold mask were removed by use of erosion routines in MATLAB. $T_{2e}$ values of the remaining voxels in the mask were used for calculating the $T_{2e}$ statistics. To make the comparison between single-B and multi-B images accurate, we only selected the voxels that were present in both eroded masks from single-B and multi-B images to calculate and compare $T_{2e}$ statistical summaries. In this manner, effects of artifacts present outside the phantom boundaries due to, e.g., partial volume averaging, fringe field effects, or possible truncation artifacts are not taken into account when $T_{2e}$ statistics are compared.

## III. RESULTS

In Figs. 3(a)–3(d), two-dimensional cross-sections of the 3D intensity and $T_{2e}$ images are shown for the vertical slice passing through the center of the phantom image. Comparing images to the phantom shape from Fig. 1(a), the cusps on the two sides of the liquid surface are visible in both intensity and $T_{2e}$ images in both acquisition methods. This observation indicates that the imaging bandwidth was sufficient for both methods so that truncation of data on the projection periphery was avoided. Nonetheless, single-B images are noisy, especially on the periphery close to the fringe field of the resonator. Single-B and multi-B images contain artifacts

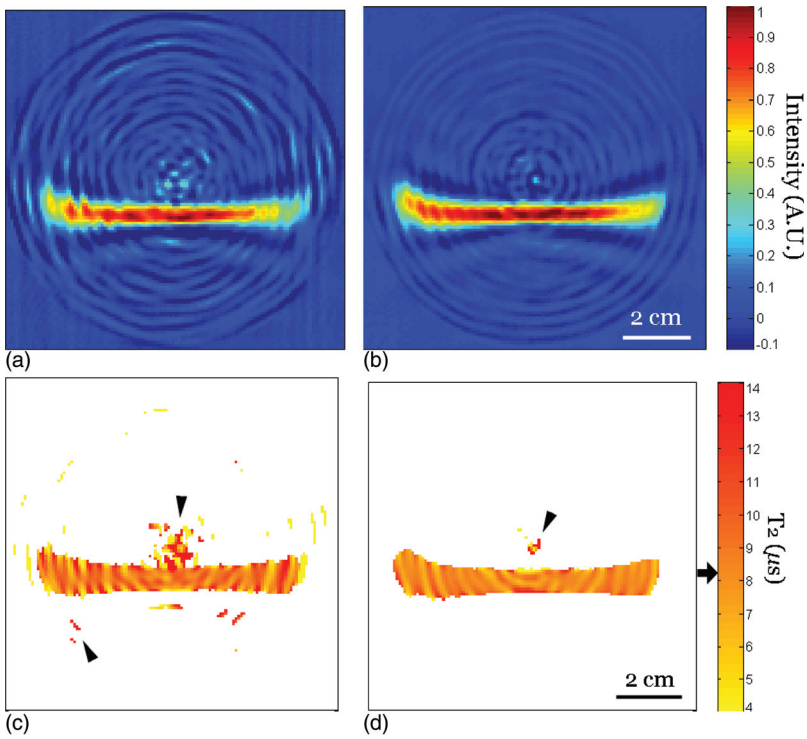


FIG. 3. (a) The single-B first $\tau$ intensity slice, passing vertically through the phantom image center. The field of view is 10 cm. (b) The same slice as in (a), from the multi-B first-$\tau$ intensity image. The single-B and multi-B images are normalized according to the maximum signal from the AWF at the central frequency. (c) $T_{2e}$ image with 15% fitting selection threshold from the single-B acquisition. Arrowheads point at image artifacts at the center and periphery. (d) Similar to (c), from multi-B acquisition, with the arrowhead indicating the center artifact. The arrow on the right points at the reference value of $T_{2e}$ obtained from nonimaging condition, with otherwise similar acquisition parameters (8.2 $\mu$s).

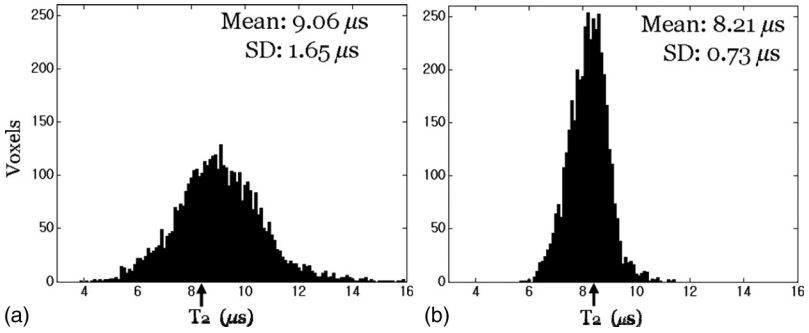


FIG. 4. (a) Distribution of $T_{2e}$ values of the single-B image voxels in the overlap mask. (b) Distribution of $T_{2e}$ values of the multi-B image voxels in the overlap mask. The small arrows indicate the reference $T_{2e}$ measured under nonimaging conditions (8.2 $\mu$s). Total number of voxels: 4271.

at the center of the image matrix as well. These center artifacts often arise from low frequency noise components or baseline fluctuations. The size of these artifacts is considerably larger in the single-B image, resulting in corruption of central regions in the $T_{2e}$ image.

The uncertainties for $T_{2e}$ values in the voxels common to the single-B and multi-B images were 1.65 $\mu$s and 0.73 $\mu$s, respectively. Therefore, switching to multi-B resulted in more than a two-fold enhancement of the $T_{2e}$ resolution. The distributions of the $T_{2e}$ values for the 4271 overlap voxels in the two images are shown in Fig. 4.

Although it was not crucial for this study, we also examined the spatial resolution for single-B and multi-B images by using the edge spread function fitting method;[29] 2.1 mm (0.3 mm standard deviation) and 1.9 mm (0.3 mm standard deviation) were obtained for single-B and multi-B images, respectively. This result is expected due to the size of the voxel (0.78 mm) and the Ram-Lak reconstruction filter cutoff (0.5) as main bottlenecks in the spatial resolution of the images. Two millimeters is a typical spatial resolution for other *in vivo* physiologic imaging modalities, e.g., positron emission tomography. Clearly, the multi-B resolution was not inferior to that of the single-B image.

## IV. DISCUSSION

We have demonstrated that the multiple-stepped Zeeman field bandwidth extension method can improve the acquisition of ESE images of large objects. The multi-B acquisition reduced the acquisition time by about 24%, due to the smaller number of averages needed for the baseline signal: each baseline signal is treated like a subprojection in terms of the number of echo averages, and multifield bandwidth extension for baseline signals was not required.

The multi-B intensity and $T_{2e}$ images were superior to the single-B image, with the $T_{2e}$ uncertainty reduced by more than a factor of 2. For *in vivo* imaging, the oxygen partial pressure is proportional to the change in the inverse of the trityl transverse relaxation time, i.e., $\Delta R_{2e}$. Therefore, a reduction in the $T_{2e}$ uncertainty by a factor of 2 is equivalent to a similar enhancement in the oxygen tension resolution. Based on calibration data published for the Finland trityl oxygen-versus-line width broadening,[18,30] single-B and multi-B images have $pO_2$ resolutions of about 6.3 and 2.8 Torr, respectively.

Based on visual inspection, multi-B images have substantially reduced artifacts. This benefit is partly due to large AWF corrections on the projection periphery in the single-B acquisition, which cause amplification of noise in frequencies far from the center. Along with the effects of angular interpolation, large AWF corrections can cause ring like artifacts on the image periphery. Lesser artifacts in the multi-B image center are due to smaller baseline effects, because of a lower radiofrequency pulse power. We have observed that reduced applied pulse power results in a proportionally smaller baseline spurious signal. Although the baseline signal is measured every four full projections and subtracted, residual effects due to temporal fluctuations in the baseline cause artifacts in the image center. Reduction of the applied pulse power for multi-B therefore results in less intense image center artifacts. For *in vivo* imaging, lower pulse power is also advantageous because of safety limits on the amount of electromagnetic energy that can be deposited in the tissue during an imaging session.

The multi-B bandwidth extension might be useful in other time-domain EPR imaging modalities as well. For example, in the single-pulse free induction decay projection-based EPR imaging technique,[31] this method may improve the image quality when multicentimeter samples are imaged. The advantages might not be as great as in the case of spin-echo EPR, though, because (1) the FID acquisition generally has a larger bandwidth, using only a single 90° excitation pulse, and (2) the higher resonator quality factor can prolong the resonator dead time, thereby distorting the FID signal that is detected shortly after the excitation pulse. On the other hand, for pure phase-encoding EPRI techniques such as Single Point Imaging,[4] also referred to as Constant Time Imaging, the frequency bandwidth limitation becomes less restrictive, and image acquisition is usually done without applying Zeeman offsets.

Another way that the multi-B technique can be utilized is for longitudinal relaxation ($T_{1e}$) studies, e.g., the inversion recovery EPR oxygen imaging technique that is currently being developed in our lab. Similar to the spin-echo imaging, the inversion recovery also needs at least two pulses: one 180° inversion pulse, followed by a 90° pulse to rotate the remaining magnetization into the transverse plane for detection. In an acquisition machine optimized for spin-echo imaging, such as ours, one may be better off using the

inversion recovery spin-echo technique, where a 180° refocusing pulse is added to the end of the pulse sequence, and the resulting echo signal is detected, diminishing the effect of dead time. Here, the use of multi-B is better justified because of the cumulative bandwidth limitations posed by all three applied radiofrequency pulses.

The multi-B acquisition technique was studied here in a setting different from that used for the study of high resolution capabilities of the spin-echo EPRI technique and potentially with more important medical applications. As noted above, different hardware and power conditions were used. The use of lower power with this technique implies a lower specific absorption rate (SAR) for living tissue. It implies a more efficient use of the applied power for oxygen imaging. The multi-B technique as described here may enable the application of pulse EPR oxygen imaging to objects with sizes relevant to the eventual measurement of oxygen images in human tumors. The larger sample and resonator used here, considering the distortional effects of larger resonators, as well as the reduction of power deposition with simultaneous improvement of the transverse relaxation time variance indicate that, under the conditions of a large sample size, the multi-B technique substantially improves the spin-echo EPR oxygen image quality.

## V. CONCLUSIONS

The multi-B ESE bandwidth expansion technique proved to be suitable for imaging of samples of large physical size, a size for which the object prevents efficient encoding of the spatial data into frequency in a single step. The eventual application of this imaging technique is to confined portions of human anatomy selectively infused with a spin probe. The multi-B technique is one step toward this goal.

## ACKNOWLEDGMENT

This work was supported by NIH Grants Nos. P-41 EB002034 and R01-CA-98575.

[a]Author to whom correspondence should be addressed. Electronic mail: h-halpern@uchicago.edu

[1]C. Mailer, S. V. Sundramoorthy, C. A. Pelizzari, and H. J. Halpern, "Spin echo spectroscopic electron paramagnetic resonance imaging," Magn. Reson. Med. **55**, 904–912 (2006).
[2]G. R. Eaton and S. S. Eaton, "Electron spin echo detected EPR imaging," J. Magn. Reson. **67**, 73–77 (1986).
[3]S. Subramanian and M. C. Krishna, "Time-domain radio frequency EPR imaging," *Biomedical EPR, Part A: Free Radicals, Metals, Medicine, and Physiology* (Springer-Verlag, New York, 2005) pp. 321–383.
[4]S. Subramanian, N. Devasahayam, R. Murugesan, K. Yamada, J. Cook, A. Taube, J. B. Mitchell, J. A. Lohman, and M. C. Krishna, "Single-point (constant-time) imaging in radiofrequency Fourier transform electron paramagnetic resonance," Magn. Reson. Med. **48**, 370–379 (2002).
[5]H. J. Halpern, C. Yu, M. Peric, E. Barth, D. J. Grdina, and B. A. Teicher, "Oxymetry deep in tissues with low-frequency electron paramagnetic resonance," Proc. Natl. Acad. Sci. U.S.A. **91**, 13047–13051 (1994).
[6]P. Kuppusamy, M. Chzhan, K. Vij, M. Shteynbuk, D. J. Lefer, E. Giannella, and J. L. Zweier, "Three-dimensional spectral-spatial EPR imaging of free radicals in the heart: A technique for imaging tissue metabolism and oxygenation," Proc. Natl. Acad. Sci. U.S.A. **91**, 3388–3392 (1994).
[7]P. Kuppusamy, P. H. Wang, and J. L. Zweier, "Evaluation of nitroxides for the study of myocardial metabolism and oxygenation," Magn. Reson. Chem. **33**, S123–S128 (1995).
[8]S. S. Velan, R. G. Spencer, J. L. Zweier, and P. Kuppusamy, "Electron paramagnetic resonance oxygen mapping (EPROM): Direct visualization of oxygen concentration in tissue," Magn. Reson. Med. **43**, 804–809 (2000).
[9]M. Elas, B. B. Williams, A. Parasca, C. Mailer, C. A. Pelizzari, M. A. Lewis, J. N. River, G. S. Karczmar, E. D. Barth, and H. J. Halpern, "Quantitative tumor oxymetric images from 4Delectron paramagnetic resonance imaging (EPRI): Methodology and comparison with blood oxygen level-dependent (BOLD) MRI," Magn. Reson. Med. **49**, 682–691 (2003).
[10]M. Elas, K. H. Ahn, A. Parasca, E. D. Barth, D. Lee, C. Haney, and H. J. Halpern, "Electron paramagnetic resonance oxygen images correlate spatially and quantitatively with Oxylite oxygen measurements," Clin. Cancer Res. **12**, 4209–4217 (2006).
[11]S. Matsumoto, F. Hyodo, S. Subramanian, N. Devasahayam, J. Munasinghe, E. Hyodo, C. Gadisetti, J. A. Cook, J. B. Mitchell, and M. C. Krishna, "Low-field paramagnetic resonance imaging of tumor oxygenation and glycolytic activity in mice," J. Clin. Invest. **118**, 1965–1973 (2008).
[12]H. Yasui, S. Matsumoto, N. Devasahayam, J. P. Munasinghe, R. Choudhuri, K. Saito, S. Subramanian, J. B. Mitchell, and M. C. Krishna, "Low-field magnetic resonance imaging to visualize chronic and cycling hypoxia in tumor-bearing mice," Cancer Res. **70**, 6427–6436 (2010).
[13]B. Epel, C. R. Haney, D. Hleihel, C. Wardrip, E. D. Barth, and H. J. Halpern, "Electron paramagnetic resonance oxygen imaging of a rabbit tumor using localized spin probe delivery," Med. Phys. **37**, 2553–2559 (2010).
[14]M. Afeworki, G. van Dam, N. Devasahayam, R. Murugesan, J. Cook, D. Coffin, J. H. Ardenjaaker-Larsen, J. B. Mitchell, S. Subramanian, and M. C. Krishna, "Three-dimensional whole body imaging of spin probes in mice by time-domain radiofrequency electron paramagnetic resonance," Magn. Reson. Med. **43**, 375–382 (2000).
[15]N. Devasahayam, S. Subramanian, R. Murugesan, F. Hyodo, K. Matsumoto, J. B. Mitchell, and M. C. Krishna, "Strategies for improved temporal and spectral resolution in *in vivo* oximetric imaging using time-domain EPR," Magn. Reson. Med. **57**, 776–783 (2007).
[16]K. H. Ahn, V. S. Subramanian, and H. J. Halpern, "Scaling of EPR spectral-spatial images with size of sample: Images of a sample greater than 5 cm in linear dimension," Med. Phys. **34**, 4854–4859 (2007).
[17]P. Seifi, B. Epel, C. Mailer, and H. J. Halpern, "Multiple-stepped Zeeman field offset method applied in acquiring enhanced resolution spin-echo electron paramagnetic resonance images," Med. Phys. **37**, 5412–5420 (2010).
[18]J. H. Ardenkjaer-Larsen, I. Laursen, I. Leunbach, G. Ehnholm, L. G. Wistrand, J. S. Petersson, and K. Golman, "EPR and DNP properties of certain novel single electron contrast agents intended for oximetric imaging," J. Magn. Reson. **133**, 1–12 (1998).
[19]T. J. Reddy, T. Iwama, H. J. Halpern, and V. H. Rawal, "General synthesis of persistent trityl radicals for EPR imaging of biological systems," J. Org. Chem. **67**, 4635–4639. (2002).
[20]I. Dhimitruka, O. Grigorieva, J. L. Zweier, and V. V. Khramtsov, "Synthesis, structure, and EPR characterization of deuterated derivatives of Finland trityl radical," Bioorg. Med. Chem. Lett. **20**, 3946–3949 (2010).
[21]H. J. Halpern, D. P. Spencer, J. van Polen, M. K. Bowman, R. J. Massoth, A. C. Nelson, E. M. Dowey, and B. A. Teicher, "An imaging radiofrequency electron spin resonance spectrometer with high resolution and sensitivity for *in vivo* measurements," Rev. Sci. Instrum. **60**, 1040–1050 (1989).
[22]B. Epel, S. V. Sundramoorthy, C. Mailer, and H. J. Halpern, "A versatile high speed 250-MHz pulse imager for biomedical applications," Concepts Magn. Reson. **33**(Pt. B), 163–176 (2008).
[23]V. S. Subramanian, B. Epel, C. Mailer, and H. J. Halpern, "A passive dual-circulator based transmit/receive switch for use with reflection resonators in pulse EPR" Concepts Magn. Reson. **35**(Pt. B), 133–138 (2009).
[24]R. W. Quine, M. Tseytlin, S. S. Eaton, and G. R. Eaton, "A very fast switched-attenuator circuit for microwave and RF applications," Concepts Magn. Reson. **37**(Pt. B), 39–44 (2010).
[25]E. G. Larsson, D. Erdogmus, R. Yan, J. C. Principe, and J. R. Fitzsimmons, "SNR-optimality of sum-of-squares reconstruction for phased-array magnetic resonance imaging," J. Magn. Reson. **163**, 121–123 (2003).
[26]R. K. Woods, W. B. Hyslop, R. B. Marr, and P. C. Lauterbur, "Image reconstruction," in *EPR Imaging and In Vivo EPR*, edited by G. R. Eaton, S. S. Eaton, and K. Ohno (CRC Press, Boca Raton, 1991), pp. 91–117.

[27]W. B. Hyslop, R. K. Woods, and P. C. Lauterbur, "Four-dimensional spectral-spatial imaging using projection reconstruction," IEEE Trans. Med. Imaging **14**, 374–383 (1995).
[28]J. A. Nelder and R. Mead, "A simplex method for function minimization," Comput. J. **7**, 308–313 (1965).
[29]K. H. Ahn and H. J. Halpern, "Simulation of 4D spectral-spatial EPR images," J. Magn. Reson. **187**, 1–9 (2007).
[30]I. Dhimitruka, M. Velayutham, A. A. Bobko, V. V. Khramtsov, F. A. Villamena, C. M. Hadad, and J. L. Zweier, "Large-scale synthesis of a persistent trityl radical for use in biomedical EPR applications and imaging," Bioorg. Med. Chem. Lett. **17**, 6801–6805 (2007).
[31]S. Subramanian, K. Yamada, A. Irie, R. Murugesan, J. A. Cook, N. Devasahayam, G.M. Van Dam, J. B. Mitchell, and M. C. Krishna, "Noninvasive *in vivo* oximetric imaging by radiofrequency FT EPR," Magn. Reson. Med. **47**, 1001–1008 (2002).
[32]K. H. Ahn and H. J. Halpern, "Spatially uniform sampling in 4-D EPR spectral-spatial imaging," J. Magn. Reson. **185**, 152–158 (2007).